Advanced Materials

ADVANCED MATERIALS
www.advmat.de

RESEARCH ARTICLE OPEN ACCESS

Resistance to Overdoping Allows Over 2000 S cm^{-1} Conductivity in P(g_3BTTT) With Anion-Exchange Doping

Basil Hunger[1] | Maximilian M. Horn[1] | Eva Röck[1] | Diego Rosas Villalva[1] | Lize Bynens[2,3] | Jochen Vanderspikken[2,3] | Christina Kousseff[4] | Silène Gobeil[1] | Olivier Bardagot[1,5] | Nesibe Akmanşen-Kalayci[6] | Sarah H. Tolbert[6,7] | Iain McCulloch[4] | Wouter Maes[2,3] | Demetra Tsokkou[1] | Natalie Banerji[1]

[1]Department of Chemistry, Biochemistry and Pharmaceutical Sciences, University of Bern, Bern, Switzerland | [2]Design & Synthesis of Organic Semiconductors (DSOS), Institute For Materials Research (imo-imomec), Hasselt University, Hasselt, Belgium | [3]imo-imomec, imec, Diepenbeek, Belgium | [4]Department of Chemistry, Chemistry Research Laboratory, University of Oxford, Oxford, UK | [5]CNRS, Institute of Chemistry and Processes for Energy Environment and Health (ICPEES), University of Strasbourg, Strasbourg, France | [6]Department of Chemistry and Biochemistry, University of California, Los Angeles, California, USA | [7]Department of Materials Science and Engineering, University of California, Los Angeles, California, USA

Correspondence: Demetra Tsokkou (dimitra.tsokkou@unibe.ch) | Natalie Banerji (natalie.banerji@unibe.ch)

Received: 30 November 2025 | **Revised:** 22 March 2026 | **Accepted:** 24 March 2026

Keywords: four-point-probe conductivity | high-doping regime | organic semiconductors | terahertz spectroscopy

ABSTRACT

Chemical doping of conjugated polymers significantly enhances their conductivity, making them attractive for a large range of applications. Recently, anion-exchange doping, where the dopant counterion is replaced by inorganic anions by exposure of a p-doped film to an electrolyte, has been demonstrated as an effective way to overcome the limitations of molecular dopants in terms of bulkiness, stability and energetics. Here, we demonstrate anion-exchange doping for polymers bearing oligoether side chains and report over 2000 S cm^{-1} electrical conductivity for the P(g_3BTTT) polymer. We investigate several thiophene and thienothiophene-based polymers in the high-doping regime to understand this high conductivity. We show that transport involves delocalized charges, that all generated charges participate to the transport, and that the mobility is resilient over nanometer to micrometer length scales. However, the high-doping regime also shows a trade-off between high charge density and high mobility, limiting the conductivity at excess concentrations of doubly charged species. Surprisingly, P(g_3BTTT) is resistant to this 'overdoping' effect and sustains particularly high levels of doubly charged species without drop in mobility. The exceptional conductivity of doped P(g_3BTTT) can thus be related to the high doping level that is achieved thanks to the oligoether side chains, without significant trade-off on the concomitantly high mobility.

1 | Introduction

Conjugated polymers are a unique class of materials with promising electronic, electrochemical and optical properties. Molecular doping (MD) enables conductivities exceeding 10^3 S cm^{-1}, suitable for flexible and semi-transparent electrodes, as well as thermoelectrics [1, 2]. However, many factors influence the conductivity in the doped samples: Amongst others, electrostatic effects, the micro- and mesoscale structure of the thin film, and the interactions of the polymer with the dopant [3, 4]. Even a given polymer/dopant system will show different performance depending on the doping methodology, owing to the particular miscibility of the polymer and dopant [5]. Novel strategies such as anion exchange doping (AED) can fine-tune those parameters. AED consists in exchanging the ionized p-dopant molecule with the anion of an electrolyte [6]. AED improves the thermal and chemical stability of the doped films, increases the charge density and can promote charge transport [6–12]. The ability to choose

from a wide variety of counterions facilitates the optimization of the polymer/ion affinity and of the film structure, shown to be critical factors [7]. Varying the electrolyte concentration controls the exchange efficiency entropically, allowing the use of anions where the free exchange energy is unfavourable [6, 13]. Finally, the polymer/counterion composition obtained by AED can be directly compared to electrochemical doping when using the same electrolyte [13].

High conductivity in doped polymer films relies on simultaneously high charge density and high charge mobility. 'Overdoping' is a trade-off between the two effects in the high-doping regime, where carrier-carrier repulsions and less mobile doubly charges species impede the transport [14–21]. This motivates us to explore AED for several thiophene and thienothiophene-based polymers, bearing either alkyl or oligoether side chains, in order to identify systems exempt from this limitation. We expect that alkylated thienothiophene-containing polymers such as PBTTT (poly(2,5-bis(3-alkylthiophene-2-yl)thieno[3,2-*b*]thiophene) outperform alkylated polythiophenes such as P3HT (poly(3-hexylthiophene)) in terms of charge transport, due to enhanced backbone planarity, high side chain interdigitation and tight backbone packing [22–24]. Moreover, we introduce oligoether side chains in P($g_3$2T-T) (poly[5,5′-(3,3-bis(2-(2-(2-methoxyethoxy)ethoxy)ethoxy)-2,2′-bithiophene)-*alt*-2,5-thiophene]) and P(g_3BTTT) (poly[4,4′-bis(2-(2-(2-methoxyethoxy)ethoxy)ethoxy)-(2,2′-bithiophen)-5,5'-diyl]-*alt*-[thieno[3,2-*b*]thiophene-2,5-diyl]). We have shown previously that replacing the alkyl side chains of P3HT with oligoether chains significantly enhances the conductivity in molecularly doped films [25]. This was related to improved processability, as well has to higher film polarity to screen Coulomb interactions. Additionally, we expect that the oligoether side chains enhance the polymer/counterion miscibility (especially upon AED), with a positive effect on the achievable charge density, film structure und ultimately resistance to overdoping [26]. With this strategy, we find extraordinarily high conductivities of over 2000 S cm^{-1} when P(g_3BTTT) is doped with AED. To explain the origin of this high conductivity and to formulate transferable guidelines for designing next-generation doped polymers, the high-doping regime is explored in detail, combining spectroscopic and structural characterization with long-range (four-point-probe) and short-range (terahertz) conductivity measurements.

2 | Results and Discussion

2.1 | Optimized Long-Range Conductivities of Doped Films

To delineate the impact of the backbone and side chains, we compare five polymers with thiophene (P3HT, P($g_3$2T-T)) or thienothiophene-based (PBTTT-C_{12}, PBTTT-C_{14}, P(g_3BTTT)) backbones, each carrying either alkyl or oligoether side chains (Figure 1a). According to reported ionization potentials, the polymers with oligoether side chains are more readily oxidized (Figure 1b) [27]. The dopants used are F_4TCNQ (2,3,5,6-tetrafluoro-tetracyanoquinodimethane) and magic blue (MB, tris(4-bromophenyl)ammoniumyl hexachloroantimonate) (Figure 1b) [4, 28]. Compared to F_4TCNQ, MB is a stronger oxidant, has a larger anion size, and tends to localize in more disordered regions of the polymer film, causing less structural disruption in crystalline domains [29, 30]. The neat polymer films are doped using either molecular doping (MD) or AED (Figure 1c). In our sequential MD protocol, the neat polymer film is immersed in a dopant solution in acetonitrile. With AED, both the dopant and the electrolyte salt (here TBAPF_6) are dissolved in the same acetonitrile solution. The molecular dopant first oxidizes the polymer, then the resulting reduced dopant ions are exchanged with the PF_6^- anions from the electrolyte [6, 9, 31]. To maximize the doping level while avoiding overdoping, the doping protocol is optimized for highest conductivity in each system, by varying the immersion duration and the dopant/electrolyte concentrations (Table S1).

The optimized long-range conductivities (σ_{long}) from four-point-probe measurements for each polymer/dopant system (with MD and AED) are summarized in Figure 1d and Table 1. The film thickness after doping, measured by white light interferometry, is used to calculate the conductivity, as this differs significantly from the thickness of the undoped films (Table S1). While most previous studies use the thickness of the undoped film to calculate the conductivity, Figure S1 shows the large discrepancy if the relevant film thickness after doping is used instead [36]. P(g_3BTTT) achieves the highest conductivity of 2100 S cm^{-1} when using AED with MB (0.6 mM) and TBAPF_6 (25 mM) as the electrolyte. This is amongst the highest reported conductivities for chemically doped polymers, achieved here with solution-processing and without engineered chain alignment [7, 13, 36–44]. This highly conductive system shows a good stability in ambient conditions over several days (Figure S2) and maintains about 80% of its stability over a week. We find that: (1) AED generally increases the conductivity in all investigated polymers compared to MD, (2) the polymers with oligoether side chains systematically outperform their alkylated counterparts, (3) the more planar PBTTT-like backbone surpasses the more torsionally disordered P3HT-like backbone, and 4) the stronger MB dopant leads to higher conductivity, even after AED, except for P($g_3$2T-T).

2.2 | Charge Densities of the Oxidized Species in the Doped Films

To understand those trends, we determine the charge density and the presence of different oxidized species in the doped films, using spectroscopic measurements. This is illustrated with the absorbance spectra of the P(g_3BTTT) films doped in different conditions (Figure 2a). The neutral polymer sites (designated as [0]) absorb around 600 nm and are only seen in the undoped film. The efficiency of the doping process is evident from the complete depletion of this band in all doped samples. When doped, the polymer segments can be oxidized once [1+] or twice [2+], yielding characteristic spectral signatures in the near-infrared region [18, 45–47]. The singly charged species (often referred to as polarons) show two absorption bands at 800 and >1600 nm, while the doubly charged species (referred to as polaron pairs or bipolarons depending on their spin characteristics) absorb at >1200 nm [48, 49]. The MD films doped with F_4TCNQ display additional ionized dopant peaks (880, 780, and 385 nm) [18, 50, 51], while ionized MB does not show any evident signature [4]. With AED in TBAPF_6, the

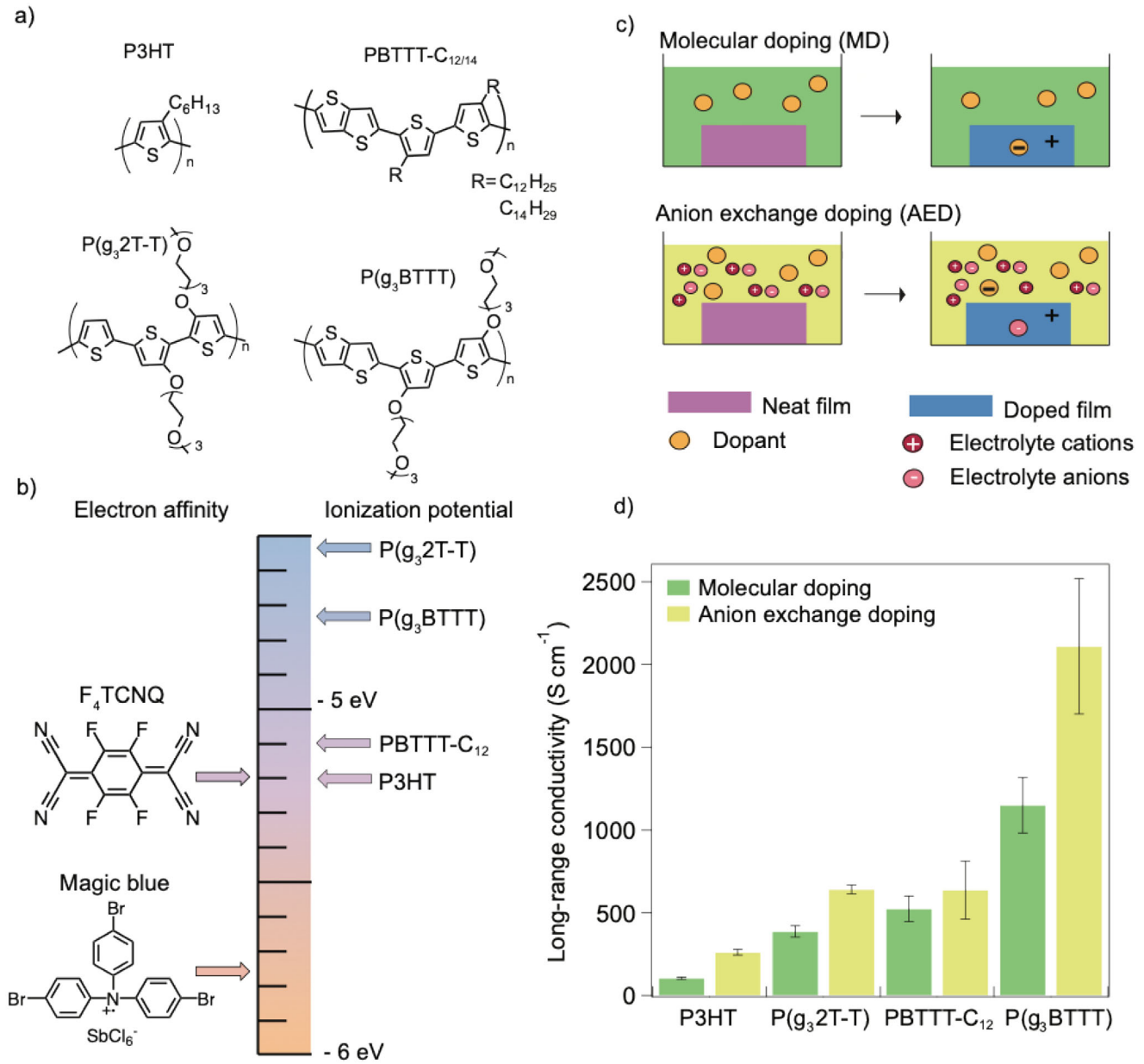

FIGURE 1 | (a) Chemical structures of the studied polymers. (b) Schematic of molecular doping (MD) by immersion in the dopant solution (top, green solution) and anion-exchange doping (AED) by immersion in the dopant plus electrolyte solution (bottom, yellow solution). (c) Ionization potentials of the different polymers and electron affinities of the dopants extracted from the literature: (P($g_3$2T-T) [32], P(g_3BTTT) [27], P3HT [33, 34] and PBTTT-C_{12} [35]). (d) Maximal long-range conductivity (from four-point-probe measurements) obtained for all polymers doped by MD (green) and AED (yellow) with magic blue (MB) in optimized conditions (see Table S1). The error bars were propagated from the standard deviation of the film thickness and sheet resistance measured over 5–10 positions on each film.

ionized F_4TCNQ peaks disappear, indicating successful anion exchange.

The spectral signatures of the neutral and charged species are quantified using spectro-electrochemistry (Figure 2b). We use the same electrolyte ($TBAPF_6$ in acetonitrile) as used in AED to ensure comparable doping conditions. A gradual evolution toward the more oxidized species is seen with increasing oxidation voltage and related to the amount of injected charge from chronoamperometry (Figures S3 and S4). The analysis yields the individual spectral signatures of the [0], [1+] and [2+] species and their absorbance cross sections (Figure 2c) [20]. The spectral components are determined for all investigated polymers in a similar manner (Figure S5). Finally, the density of the neutral and charged species in the chemically doped films is obtained by fitting the sum of the absorbance cross sections to the absorbance spectra of the doped samples (Figures S6–S18). As the conductivity depends on both the charge density and their mobility, we disentangle the two effects. The total charge density is given by: $[\text{Charge}]_{\text{tot}} = [1+] + 2\times[2+]$. The mobility ($\mu_{\text{long}}$) is then deduced according to: $\mu_{\text{long}} = \sigma_{\text{long}}/e[\text{Charge}]_{\text{tot}}$, where e is the elemental charge. This assumes that all charges participate simultaneously in the transport, as confirmed below by terahertz spectroscopy. We generally find high charge densities

TABLE 1 | Long-range conductivities (σ_{long}) from four-point-probe measurements for each optimized polymer/dopant system with MD and AED doping. Detailed doping conditions are given in Table S1, together with experimental uncertainties. Values shown here are at maximum conductivity before the overdoping regime is reached for certain polymers. The total charge density ($[Charge]_{tot}$) is obtained by adding the density of singly charged species ([1+]) to twice that of the doubly charged species ([2+]). Those densities, as well as the one of neutral sites ([0]) are found after decomposing the absorbance spectra of the doped films into the signatures of the different oxidized species. The calculated long-range mobility (μ_{long}) is obtained by dividing the conductivity by the total charge density. The relative change in film thickness (Δd/d) is the thickness difference between the doped and undoped film, divided by the thickness of the undoped film. The charge per thiophene unit (TU) is calculated from the undoped film density, Δd/d and $[Charge]_{tot}$.

	σ_{long} (S cm^{-1})	$(Charge)_{tot}$ (10^{21} cm^{-3})	μ_{long} (cm^2 V^{-1} s^{-1})	[0] (10^{20} cm^{-3})	[1+] (10^{20} cm^{-3})	[2+] (10^{20} cm^{-3})	[2+]:[1+]	Δd/d (%)	Charge/TU
P3HT									
F_4TCNQ MD	6	0.3	0.2	0.82	2.18	0.15	0.07:1	50	0.09
F_4TCNQ AED	5	0.2	0.1	0.83	2.07	0.16	0.08:1	45	0.09
MB MD	105	0.6	1.1	0.04	1.56	2.10	1.35:1	58	0.23
MB AED	262	0.9	1.7	0.05	2.65	3.37	1.27:1	−1	0.23
P($g_3$2T-T)									
F_4TCNQ MD	279	1.1	1.7	—	6.28	2.14	0.34:1	55	0.52
F_4TCNQ AED	684	1.7	2.5	—	8.85	4.18	0.47:1	4	0.57
MB MD	387	1.1	2.1	—	6.06	2.63	0.43:1	45	0.52
MB AED	641	1.9	2.2	—	9.26	4.64	0.50:1	−8	0.54
PBTTT-C_{12}									
F_4TCNQ MD	48	0.2	1.2	1.50	2.33	0.06	0.02:1	−1	0.06
F_4TCNQ AED	71	0.3	1.3	1.05	2.86	0.25	0.09:1	5	0.08
MB MD	524	0.6	5.3	0.05	2.53	1.81	0.72:1	13	0.17
MB AED	637	0.9	4.4	0.12	3.20	2.94	0.92:1	−12	0.19
P(g_3BTTT)									
F_4TCNQ MD	717	1.5	3.0	—	8.79	3.15	0.36:1	61	0.60
F_4TCNQ AED	1230	2.2	3.6	—	8.58	6.45	0.75:1	23	0.65
MB MD	1150	1.6	4.5	—	4.45	5.80	1.28:1	84	0.73
MB AED	2110	2.8	4.7	—	5.28	11.40	2.16:1	−1	0.68

of the order of 10^{20}–10^{21} cm^{-3} in all polymers (Table 1; Table S1). This surprisingly high doping regime has been confirmed in other doped polymers probed by a variety of techniques [41, 44, 52, 53]. Comparison of the different doped P(g_3BTTT) films highlights that both an increase in charge density and in the mobility lead to the impressive conductivity achieved with this polymer in optimized conditions (Figure 2d).

2.3 | Parameters Affecting the Conductivity and Charge Mobility

We start by comparing the effect of the two dopants on the interplay of charge density and mobility with MD doping. For P3HT and PBTTT-$C_{12/14}$, F_4TCNQ does not lead to complete doping and a significant density of neutral sites remains (Table 1; Table S1). In agreement with previous reports, the doping level cannot be thermally activated (Figure S19) [54]. It is limited by the small offset between the electron affinity of F_4TCNQ and the ionization potential of the polymer (Figure 1b). The lower charge density achieved with F_4TCNQ leads to lower conductivity and the mobility is also significantly reduced compared to doping with MB (Table 1). As we have shown previously for P3HT:F_4TCNQ films in this intermediate doping regime, both disorder and Coulomb trapping of charges to the ionized dopant decrease the mobility [25]. When the alkylated polymers are doped with the stronger oxidant MB, the charge density doubles, there is almost complete depletion of the neutral sites and the mobility is higher than when doping with F_4TCNQ. MB is known to preferentially locate in more disordered regions of polythiophene films, causing less morphological disruption [55]. Additionally, we expect less Coulomb trapping due to screening effects at high charge densities [56]. In the polymers with oligoether side chains, owing to their more favourable ionization potential, doping is complete with either dopant (no remaining [0] sites), and much higher charge densities are achieved than with the alkyl side chains (Table 1). We still find an increase in charge density, mobility and conductivity when using MB rather than F_4TCNQ, but the gain is marginal for P($g_3$2T-T).

Second, we investigate the impact of AED on the conductivity. Although the dopant anion is entirely replaced by PF_6^-, the

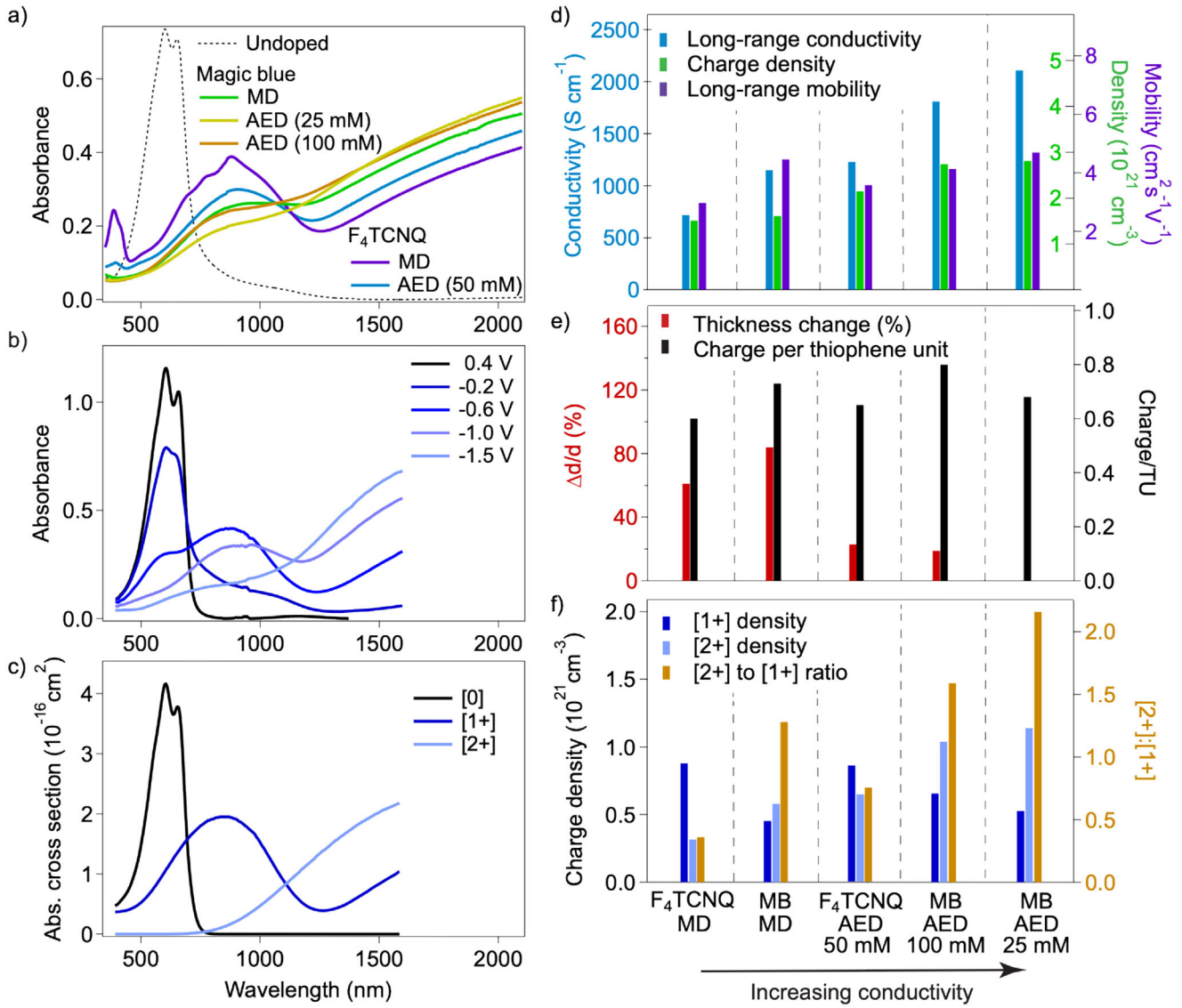

FIGURE 2 | (a) Absorbance spectra of P(g_3BTTT) films doped with F_4TCNQ or MB using molecular doping (MD) or anion-exchange doping (AED) with $TBAPF_6$/acetonitrile electrolyte at the indicated concentration. All spectra correspond to an initial film thickness (before doping) of 30 nm. (b) Spectro-electrochemistry of a P(g_3BTTT) film in $TBAPF_6$/acetonitrile electrolyte. (c) Absorbance cross section spectra of the neutral ([0]), singly charged ([1+]) and doubly charged ([2+]) species. (d) Long-range conductivity (blue), total charge density (green) and long-range mobility (purple) of the doped P(g_3BTTT) films. (e) Relative thickness change (dΔ/d) upon doping (red) and charge per thiophene unit (TU) (black). (f) Density of the [1+] and [2+] charged species (dark and light blue), and [2+]:[1+] ratio (orange).

trends between F_4TCNQ and MB are carried on to the AED samples (Table 1; Table S1). For example, there is incomplete doping with F_4TCNQ/AED for the polymers with alkyl side chains, and the charge density is generally higher with MB/AED than F_4TCNQ/AED. Moreover, the charge density systematically increases with AED compared to MD. However, this is not related to a higher doping level, but rather to the doped films being thinner with AED, as illustrated in Figure 2e for P(g_3BTTT). Measuring the dry film thickness before and after doping with this polymer reveals that the thickness increases by 60%–80% with MD (independently of the dopant), but only by 0%–20% with AED (Table 1). The film with the highest conductivity of 2100 S cm^{-1} has the same thickness as the undoped film, suggesting excellent miscibility of PF_6^- with the polymer and likely leading to minimal structural disruption. P($g_3$2T-T) shows the same behaviour, as both MD films are about 50% thicker than the undoped films, while the AED films have a similar thickness. For the polymers with alkyl side chains, the MB/AED films are also the thinnest and typically have the same thickness as before doping (Table S1). To discard the effect of the film thickness on the doping level, we calculate the charge per thiophene unit (TU) by assuming a density of 1.1 g/cm^3 in all undoped polymer films [57, 58]. This confirms that for all studied polymers, AED does not generate more charges but concentrates them in a smaller film volume (Figure 2e; Table 1), with a positive impact on the charge density and often also on the mobility.

We now look at the nature of the charges. Even if AED does not increase the overall doping level, the absorption spectra of the doped P(g_3BTTT) films show a significant redistribution between

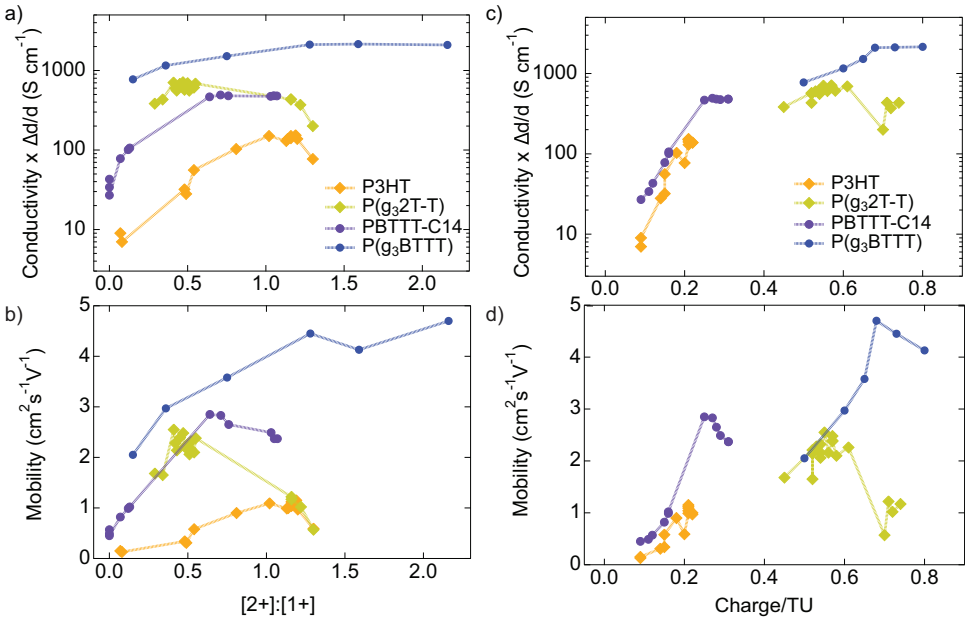

FIGURE 3 | (a) Long-range conductivity of the doped polymer films as a function of the doubly-to-singly charged species ratio ([2+]:[1+]). The conductivity was corrected for the change in film thickness upon doping to discard any thickness effects (with minimal impact on the trends, Figure S20a). (b) Long-range mobility of the doped polymer films as a function of the doubly-to-singly charged species ratio ([2+]:[1+]). (c) Long-range conductivity (corrected for the change in film thickness upon doping) of the doped polymer films as a function of charge per thiophene unit (TU). (d) Long-range mobility of the doped polymer films as a function of charge per thiophene unit (TU). The details of the doping conditions are given in Table S1, and similar graphs for PBTTT-C_{12} and another P3HT batch are shown in Figure S20.

the [1+] and [2+] species depending on the doping conditions (Figure 2a). Using MB rather than F_4TCNQ for MD doping increases the [2+]/[1+] ratio (Figure 2f). This is related to the higher oxidation strength of MB and its preferential location in disordered film regions, where the formation of [2+] is favoured [20]. AED further increases the density of [2+] species compared to the corresponding MD-doped films. The higher [2+]/[1+] ratio with MB and AED doping is observed in all polymers (Table 1; Table S1). However, the impact on the conductivity is not the same. For P(g_3BTTT), the sample with the record conductivity of 2100 S cm^{-1} has the highest [2+]/[1+] ratio (Figure 2f). Surprisingly, both the conductivity and the mobility of doped P(g_3BTTT) keep increasing with the [2+]:[1+] ratio (Figure 3a,b). In contrast, the other polymers reach a much lower [2+] level and show an increase followed by a drop of the conductivity when [2+]:[1+] >1 (Figure 3a). This known overdoping effect is related to a decrease in mobility at high [2+] densities (Figure 3b), caused by inferior transport and/or enhanced disorder when [2+] species predominate [17–21]. It explains why P($g_3$2T-T) doped with F_4TCNQ performs similarly or better than with MB, where the high [2+] density overdopes the film (Table 1). The small scatter in the plots of Figure 3a, in spite of largely different doping conditions between the points, highlights the [2+]:[1+] ratio as a primary factor in determining the conductivity [18, 37], overriding electrostatic and structural trends due to the counterion (Table S1). Thus, the resistance of P(g_3BTTT) to strong doping conditions and high [2+] levels sets this polymer apart and explains its exceptional performance.

As the [2+]:[1+] ratio does not necessarily reflect the overall doping level and charge density, we also report the conductivity and mobility as a function of charge per thiophene unit (Figure 3c,d). Independently of the nature of the charge, densities approaching a charge on every TU cause severe carrier-carrier repulsions and a dramatic effect on the electrostatic landscape [14–16]. The polymers with alkyl side chains and less favourable oxidation potential (P3HT, PBTTT-C_{14}) reach much lower loping levels. Only PBTTT-C_{14} reaches a charge/TU level above 0.2, where a saturation in the conductivity and drop in mobility are evident. The polymers with oligoether side chains (P($g_3$2T-T), P(g_3BTTT)) are doped much more heavily, showing that the side chain engineering is an effective strategy to increase the doping level. Here, deteriorated transport sets on above 0.6–0.7 charge/TU. Again, P(g_3BTTT) outperforms P($g_3$2T-T) due to a higher charge mobility and less pronounced conductivity drop at the highest doping levels.

2.4 | Short-Range Terahertz Conductivity

We investigate the transport properties in more detail using terahertz (THz) spectroscopy. Here, a single-cycle THz pulse interacts with the mobile charges in the doped polymer film only during the pulse duration of about 1 ps, which probes the charge transport on the nanometre length scale. Such a short pulse contains a broad range of frequencies, and these measurements yield the complex conductivity spectra of the doped films (Figure S21). The real value at 1 THz corresponds to the short-range conductivity (σ_{short}). We have recently reported the concept of 'distance resilience' ($= \sigma_{long}/\sigma_{short}$) to define how much of the nanometre conductivity is maintained when going to millimetre distances [25]. Here, we find that for all investigated polymers, the optimized MD and AED samples have a distance resilience of ≈ 1 (Figure 4a). The near-identical σ_{short} and σ_{long}

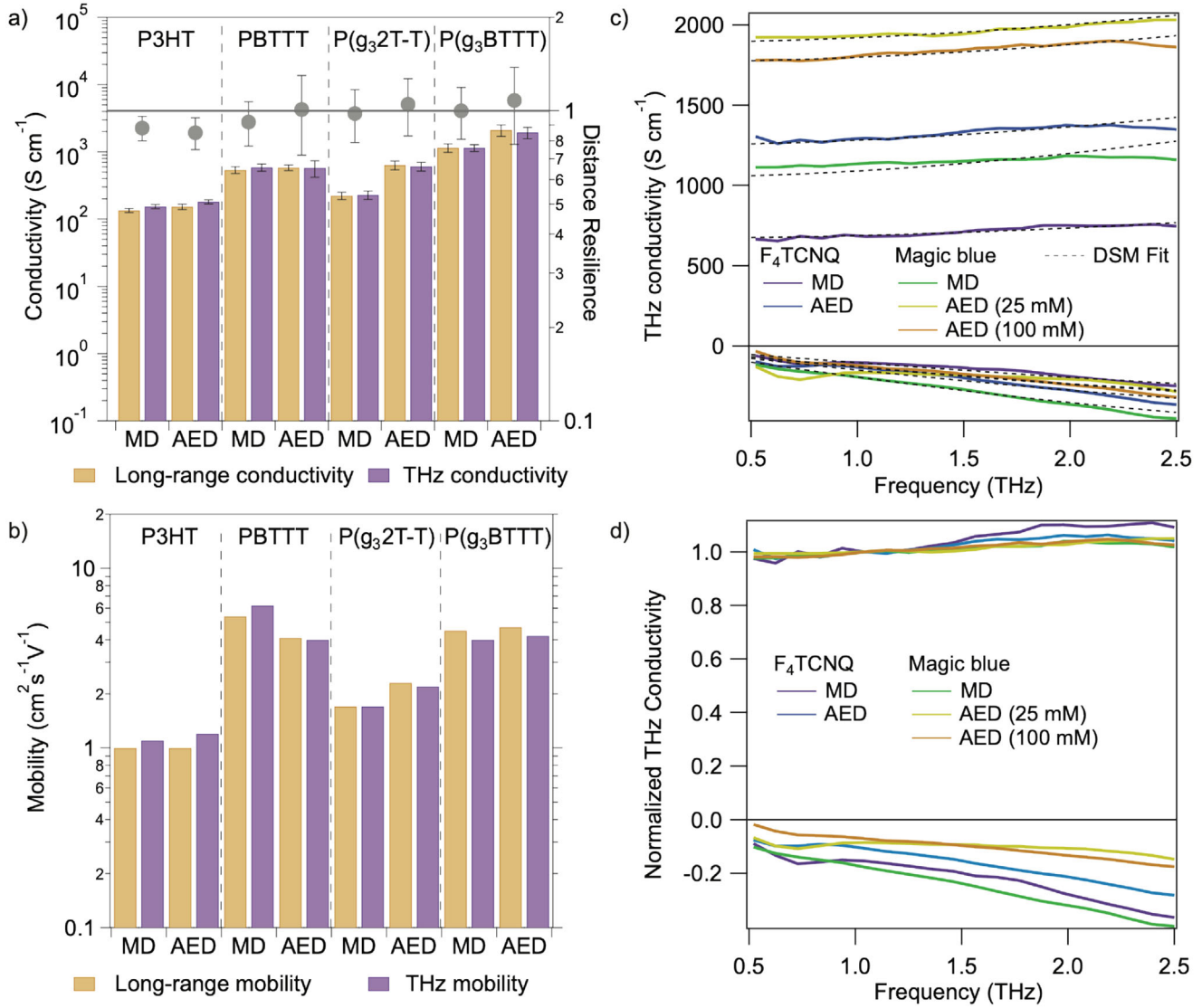

FIGURE 4 | (a) Long-range conductivity (orange bars) and short-range conductivity at 1 THz (purple bars) of the different polymer films (P3HT, PBTTT-C_{12}, P($g_3$2T-T) and P(g_3BTTT) doped to the highest level using either molecular doping (MD) or anion-exchange doping (AED), with magic blue dopant (except for P($g_3$2T-T), where F_4TCNQ yielded a higher conductivity). The distance resilience is the ratio of the long-range to short-range conductivity. The error bars were propagated from the standard deviation of the film thickness and conductivity measured over 5–10 positions on each film. (b) Corresponding long-range mobility and effective THz mobility (calculated by the Drude-Smith model, DSM). (c) Complex THz conductivity spectra of the P(g_3BTTT) films doped with F_4TCNQ or MB using MD or AED with $TBAPF_6$/acetonitrile electrolyte (same films as Figure 2a). The black dotted lines are fits using the DSM. (d) THz conductivity spectra normalized at 1 THz with the imaginary part scaled accordingly.

values for the highly doped samples confirm the measured four-point-probe conductivities and highlight that no loss in charge transport occurs over several orders of magnitude in distance. This contrasts with previous reports at lower doping levels, where the conductivity and THz hole mobility in conjugated polymers is significantly higher than the long-range one [59]. Our results show that a high-doping regime is reached, where the transport does not suffer from structural or energetic traps that disrupt conductive pathways over longer distances, such as disorder, domain/grain boundaries or Coulomb binding to the anion.

The degree of charge 'localization' caused by those effects reflects in the shape of the THz conductivity spectra, namely in the extent of the negative imaginary part and the slope of the real part, as we have demonstrated by kinetic Monte Carlo simulations [25]. To compare the complex conductivity spectra, their real part is normalized, and the imaginary part is scaled accordingly. For all doped P(g_3BTTT) films (Figure 4c,d), we find a flat real conductivity spectrum and a small negative imaginary part compared to the real part (Im/Re at 1 THz < 0.15). The high distance resilience reflects in the almost flat real conductivity spectra, as the extrapolated THz conductivity at zero frequency is similar to the long-range one. In general, slower transport events contribute at low THz frequencies, while faster transport events contribute at high THz frequencies. For our highly conductive polymers with a distance resilience of ≈ 1, similar transport events contribute at both low and high THz frequencies. Moreover, the small Im/Re confirms that the charges are delocalized and not energetically or morphologically confined, in agreement with the high conductivity and excellent distance resilience. In contrast,

TABLE 2 | Long-range conductivities (σ_{long}) from four-point-probe measurements and short-range conductivities (σ_{short}) from THz spectroscopy for different polymer/dopant systems with MD and AED doping. Detailed doping conditions are given in Table S1. Films may differ from the ones in Table 1, so conductivities are not necessarily exactly the same. The distance resilience is the ratio $\sigma_{long}/\sigma_{short}$. The total charge density ($[Charge]_{tot}$) is from the absorbance spectra as explained before. The same values ($[Charge]_{DSM}$) are used to fit the complex THz conductivity spectra with the Drude-Smith model (DSM), showing that all generated charges contribute to the conductivity. The DSM parameters are the scattering time (τ_{DSM}) and the localization parameter (C_{DSM}). The effective THz mobility (μ_{DSM}) is deduced from τ_{DSM} and C_{DSM} and compared to the long-range mobility (μ_{long}). Table S2 shows the short- and long- range conductivities with the experimental uncertainty.

	σ_{long} (S cm^{-1})	σ_{short} (S cm^{-1})	$\sigma_{long}/\sigma_{short}$	$(Charge)_{tot}$ (10^{21} cm^{-3})	$(Charge)_{DSM}$ (10^{21} cm^{-3})	τ_{DSM} (fs)	C_{DSM}	μ_{long} (cm^2 V^{-1} s^{-1})	μ_{DSM} (cm^2 V^{-1} s^{-1})
P3HT									
MB MD	135	154	0.88	0.9	0.9	8.1	−0.87	1.0	1.1
MB AED	153	181	0.85	0.9	0.9	7.0	−0.83	1.0	1.2
P($g_3$2T-T)									
F_4TCNQ MD	223	228	0.98	0.8	0.8	8.2	−0.80	1.7	1.7
F_4TCNQ AED	638	610	1.05	1.7	1.7	8.3	−0.74	2.3	2.2
MB MD (overdoped)	107	191	0.56	1.2	1.2	7.5	−0.87	0.6	1.0
MB AED (overdoped)	432	464	0.93	2.3	2.3	6.8	−0.82	1.2	1.3
PBTTT-C_{12}									
MB MD	540	588	0.92	0.6	0.6	19.0	−0.68	5.4	6.2
MB AED	584	578	1.01	0.9	0.9	10.8	−0.65	4.1	4.0
P(g_3BTTT)									
F_4TCNQ MD	717	684	1.05	1.5	1.5	11.3	−0.76	3.0	2.8
F_4TCNQ AED	1230	1280	0.96	2.2	2.2	12.5	−0.72	3.6	3.6
MB MD	1150	1150	1.00	1.6	1.6	15.5	−0.75	4.5	4.0
MB AED (100 mM)	1810	1794	1.01	2.7	2.7	11.8	−0.67	4.1	4.1
MB AED (25 mM)	2110	1950	1.08	2.8	2.8	11.9	−0.66	4.7	4.2

we found Im/Re ≈ 1.3 for a P3HT:F_4TCNQ film with lower doping level, low conductivity (0.2 S cm^{-1}) and distance resilience of only 4% [25].

Analysis of the THz spectra with the phenomenological Drude-Smith model (DSM) further quantifies the transport. This extracts the density of conductive charges ($[Charge]_{DSM}$), the scattering time (τ_{DSM}, representative of ballistic transport in fully conjugated chain segments) and the localization parameter (C_{DSM}, encompassing the structural and energetic effects discussed above). Importantly, we are always able to fix $[Charge]_{DSM}$ to the value of $[Charge]_{tot}$ obtained from the absorbance spectra, showing that all generated charges are simultaneously conductive (Table 2). In polymer films with a lower doping level, only a fraction of charges (5%–20%) contributes to the charge transport [18, 56]. We find that τ_{DSM} is higher and C_{DSM} smaller (i.e. less negative) for the more planar polymers with thienothiophene-based backbones, pointing to more delocalized transport (Table 2). This is further supported by temperature-dependent THz conductivity measurements for the four highly conductive polymers doped with MB/AED (Figure S22). The conductivity at low temperatures (≈15 K) is non-zero, evidencing that both hopping-like and metallic-like transport take place. Importantly, we find that the doped thienothiophene-based polymers, which also have a smaller C_{DSM} than the thiophene-based polymers, show a weaker dependence of the conductivity on temperature, confirming more delocalized transport. For each polymer, the doped samples with the highest conductivity also show the smallest C_{DSM}, with particularly clear trends in the doped P(g_3BTTT) films (Figure 4d and Table 2). For P($g_3$2T-T) doped with MB (both MD and AED), the films used for THz spectroscopy were overdoped, indicating that the excess [2+] species lead to charge localization (Table 2; Table S1). For all other systems, AED reduces the localization parameter, corroborating the positive effect of AED on the charge transport. The short-range mobilities, calculated from the DSM parameters, perfectly match the long-range mobilities and their trends (Figure 4b). This further confirms the robustness of our results and the ability of the highly doped samples to sustain transport from the nanoscopic to the microscopic scale.

2.5 | Structural Characterization

Finally, we investigate the effect of structure for the four polymers doped with MB, using the MD and AED methods in conditions yielding optimal conductivity. The grazing incidence wide angel

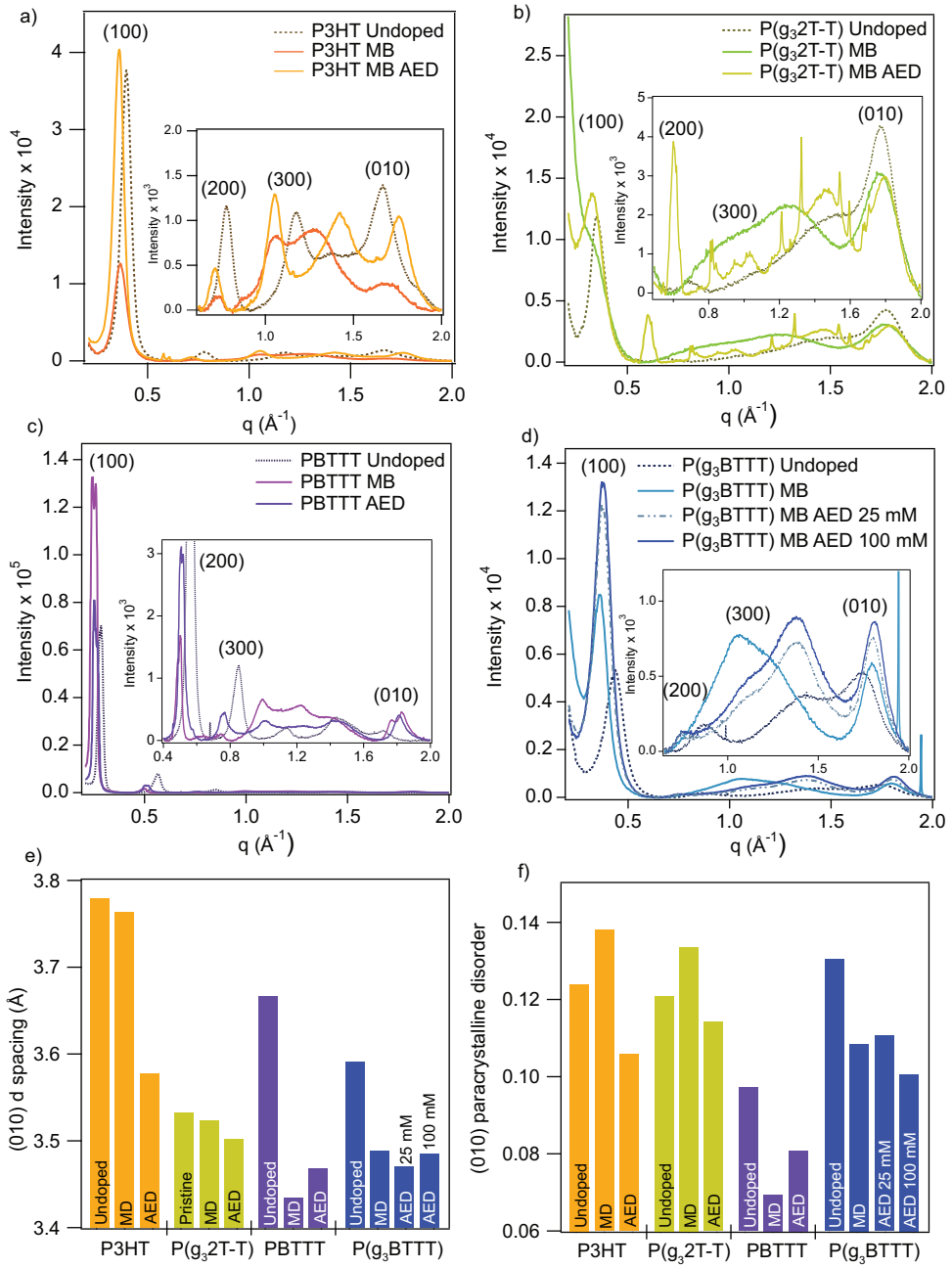

FIGURE 5 | (a–d) Radial integrations (between 0–89 chi angle) from the GIWAXS data of undoped, MB/MD doped, and MB/AED doped polymers for (a) P3HT, (b) P($g_3$2T-T), (c) PBTTT-C_{14}, and (d) P(g_3BTTT). (e) (010) d spacing for all samples. (f) Paracrystalline disorder calculated from the (010) peak width for all samples.

x-ray scattering (GIWAXS) data indicate that all polymers have the expected edge-on orientation [27, 60, 61], except for P($g_3$2T-T) [32, 62], which shows a mixture of edge-on and face-on conformations (see raw 2D diffraction plots in Figures S23–S26). In the thickness-normalized radial integrations, all samples show a series of diffraction peaks labeled (h00) at low angle, that correspond to the lamellar spacing, and a single peak at higher angle, labeled (010), that corresponds to the π-stacking distance (Figure 5a-d). The undoped polymers with alkyl side chains show higher (100) scattering intensity than their oligoether counterparts (Figure S27), pointing to higher crystallinity related to better side chain ordering. Upon doping with MB or MB/AED, the lamellar peaks shift to lower q values in all polymers, indicating a lattice expansion. This shows that, at our high doping levels, the MB dopant as well as the AED anion intercalate among the side chains of the crystalline polymer regions and are not just present in amorphous domains. In contrast, the π-stacking distance decreases for all doped polymers due to backbone planarization during doping, in agreement with previous reports (Figure 5e) [11, 63, 64].

For the thiophene-based polymers, MB-doping increases the paracrystalline disorder (g) of the (010) peak and reduces the crystallinity, but it has the opposite effect on the thienothiophene-based polymers (Figure 5f; Figure S27). This is likely because the $SbCl_6^-$ anion is better able to fit into the PBTTT-family

crystals. AED on the contrary, decreases g for all polymers and increases the (100) peak amplitude compared to the undoped case, indicating an improved structural order due to a crystallization process during AED doping with PF_6^- anion. The (010) peaks of the doped thienothiophene-based polymers show lower g than their thiophene counterparts, suggesting a more conformationally rigid backbone and agreeing with the higher charge mobility in doped P(g_3BTTT) compared to P($g_3$2T-T) (Figure 4b). PBTTT-C_{14} shows overall higher crystallinity and ordering than the other polymers, but both the structure and mobility slightly deteriorate with MB/AED, possibly linked to the onset of overdoping (Figures 3 and 5; Figure S27). Although P(g_3BTTT) reaches over twice the doping level of PBTTT-C_{14}, both doping methods (MB and MB/AED) lead to structural improvements with respect to the undoped polymer. We thus evidence that P(g_3BTTT) is also structurally resistant to overdoping effects at high charge densities and [2+]:[1+] ratios.

3 | Conclusion

In summary, we demonstrate here the effectiveness of anion-exchange doping for polymers bearing oligoether side chains and report >2000 S cm^{-1} conductivity for P(g_3BTTT). We investigate thiophene and thienothiophene-based polymers in the high-doping regime, where transport involves delocalized charges, carrier-screening effects dominate so that all generated charges participate to the transport, and the mobility is resilient over nanometer to micrometer length scales. In this regime, we recognize the [2+]:[1+] ratio as the key factor determining the conductivity of a given polymer, even overriding electrostatic and structural trends due to the precise nature of the counterion. We identify 'overdoping' as a critical limitation to reach high conductivities in chemically doped polymers. At high doping levels and even more if the density of [2+] doubly charged species is high, overdoping can severely limit the conductivity of doped conjugated polymers and imposes a trade-off between high charge density and high mobility. Interestingly, P(g_3BTTT) is largely exempt from this effect.

We show that a stronger molecular dopant (magic blue) increases the doping level and concentration of [2+] species compared to the weaker dopant F_4TCNQ. Careful optimization of the dopant concentration and immersion time is necessary to maximize the charge density without reaching the overdoping regime for P3HT, P($g_3$2T-T) and PBTTT-$C_{12/14}$. The doping level (charge per thiophene unit) is pre-determined by the molecular dopant and does not increase with anion exchange. However, especially with oligoether side chains, the anion-exchange films have a similar thickness as the undoped films while the molecular-doped films are much thicker. This concentrates the charges in a smaller volume (higher charge density) and is structurally favourable as seen by an increase in the mobility and charge delocalization (probed by THz spectroscopy). Moreover, the anion-exchange tends to re-distribute the charges toward a higher [2+]:[1+] ratio, which benefits the conductivity until a ratio of ≈ 1 is reached, but then causes a severe drop. Only P(g_3BTTT) is resistant to overdoping, although the oligoether side chains allow much higher doping levels. Even a high excess of [2+] species keeps boosting the charge mobility, which is already intrinsically high due to the planar thienothiophene-bithiophene backbone. Merely when the charge density per thiophene unit approaches 1, carrier-carrier interactions cause a slight decrease in the mobility, but this sets on at much higher doping levels and is less pronounced than for the other polymers. Further structural and theoretical work is ongoing to explain the resistance to overdoping in P(g_3BTTT). We hypothesize that it might be related to the torsionally constrained backbone, with S—O interactions enhancing conformational rigidity even when high densities of [2+] species and counterions are present in crystalline film regions [27]. GIWAXS measurements show that the structural ordering of P(g_3BTTT) improves with respect to the undoped polymer, even in the very high doping regime. The exceptional performance of doped P(g_3BTTT) can thus be related to the high doping level that can be achieved in this material without significant trade-off on the concomitantly high mobility.

4 | Experimental Methods

4.1 | Materials

P3HT was purchased from Ossila with a regioregularity of 97.6%, Mn = 29 kg/mol and PDI = 2.1. PBTTT-C_{12} was purchased Sigma–Aldrich with a PDI of 2–3 and Mn = 40–120 kg/mol. PBTTT-C_{14} was synthesised according to literature [65]. The synthetic route of P(g_3BTTT) was also described previously [66]. P($g_3$2T-T) was synthesized as previously described [32]. F_4TCNQ was purchased from Ossila and magic blue from Sigma–Aldrich.

4.2 | Film Preparation and Doping

Ultra-flat quartz coated substrates (from Ossila) were used for the long-range conductivity and absorbance measurements, while films were spin-coated on ITO-coated substrates (from Ossila) for chronoamperometry measurements. Fused quartz substrates (from Technical Glass Products) were used for the THz measurements. All substrates were washed by sonicating for 15 min in a 1% vol. Hellmanex solution, followed by sonication for 5 min in water, then 10 min in acetone, and finally 15 min in isopropyl alcohol. The substrates were dried with nitrogen and transferred to a UV-ozone cleaner (Ossila) for 20 min. Neat polymer films were spin-coated under inert conditions in the glovebox. For P(g_3BTTT), 9 g/L of the polymer was dissolved in chloroform and stirred overnight at 45°C to ensure good dissolution. The polymer was spin-coated at 2000 rpm. 9 g/L of PBTTT-C_{14} was dissolved in 1,2-dichlorobenzene and was stirred for 3 h at 80°C and spin-coated at 1000 rpm. 20 g/L PBTTT-C_{12} was dissolved in 1,2-dichlorobenzene and stirred for 2 h at 120°C and then 1 h at 100°C. Neat films were spin-coated at 1000 rpm and were annealed at 180°C for 20 min in the glovebox. For P3HT, a chlorobenzene solution of 10 g/L was stirred at 70°C for 2 h. The films were spin-coated at 1000 rpm. P($g_3$2T-T) was dissolved in chloroform (5 g/L) and stirred at 45°C overnight before spin-coating at 750 rpm. Subsequently, the neat polymer films were doped in the glovebox via molecular or anion exchange doping, whereby the films were immersed in an acetonitrile solution of dopant or a mixture of dopant and $TBAPF_6$, respectively. The dopant and electrolyte concentrations as well as the immersion time are listed in Table S1. Finally, the doped films were cleaned from excess electrolyte by rinsing with acetonitrile and spinning off the solvent at 4000 rpm.

4.3 | Steady-State Absorbance and Film Thickness

The steady-state absorbance spectra were recorded with a Lambda 950 spectrophotometer (Perkin Elmer) equipped with a 150 mm integrating sphere (to minimize scattering effects) or with a Cary 6000i UV—vis–NIR spectrophotometer. For the P($g_3$2T-T) films, the sample chamber of the spectrometer was purged with nitrogen due to their sensitivity to atmospheric conditions. The film thickness was measured using a white light interferometer (Bruker CountourGT). Measurements were performed in phase shifting interferometry (PSI) mode. For each film, several measurements were taken at different sample positions (at least 3 different locations with 3 measurements each). The absorbance spectra were recorded for the undoped films and the same films after doping (Figures S28–S39). The film thickness was also determined before and after doping of each film. In some cases, the thickness of the undoped film was deduced from the absorbance and the absorbance-thickness calibration curve (Figure S40), to minimize film exposure to air.

4.4 | Four-Point-Probe Long-Range Conductivity

To measure the long-range conductivity (σ_{long}), a four-point probe setup from Ossila was used in air at room temperature. For the measurement, a current is applied over the outer two electrodes, and the voltage drop between the inner electrodes is measured. The difference in voltage, film dimension and the thickness of the film is then used to determine the conductivity. For each film, several measurements (at least three) in different positions on the sample were taken.

4.5 | Spectro-Electrochemistry and Chronoamperometry (Absorbance Cross Sections)

For spectro-electrochemistry, the neat films were spin-coated onto ITO-coated glass substrates. A film area of 0.3 × 0.4 mm was delimited with Kapton tape (excess polymer was removed using a Q-Tip) and exposed to the electrolyte (degassed 100 mM $TBAPF_6$ in acetonitrile) in a solvent-resistant cell containing an Ag/AgCl counter-electrode. A PalmSens4 bipotentiostat was used to apply voltage steps of 0.1 V over a range of + 0.4 to −1.2 V while recording current transients. Absorbance spectra at different applied voltages were recorded with two detectors from Ocean Optics (visible and near-infrared from 400 to 1700 nm). For the light source, a HL 2000 lamp (Ocean Optics) was used. To extract the cross sections for neutral [0], singly charged [1+] and doubly charged [2+] species, multivariate curve resolution (MCR) analysis was used to decompose the absorbance data from the spectro-electrochemistry [20]. This allows to determine the absorbance of the separate species at the peak maximum at each applied voltage, without spectral overlap with the other species. The current transients were integrated to yield the injected charges per voltage step which was then summed up to yield the total integrated charge density (Figure S3). This was plotted against the absorbance of the charged species, assuming a one-to-one conversion between the injected current and the induced charges (Figure S4). The curves were fitted (range depicted by a black line) to get the absorbance cross section of [0] and [1+]. Finally, the absorbance of the [2+] was plotted against the injected [2+] density, yielding the [2+] absorbance cross section (Figure S5).

4.6 | Charge Densities and Charge Per Thiophene Unit

The absorbance cross section spectra were fitted to the absorbance spectra of the doped polymer films in order to determine the concentration of the [0], [1+] and [2+] species (as well as [F4TCNQ$^-$] if needed), Figures S6–S18. The total charge density ($[Charge]_{tot}$) was calculated by adding the density of singly charged species ([1+]) to twice that of the doubly charged species ([2+]). To estimate the doping level, we considered the number of charges per thiophene unit (TU), counting 1 ring per P3HT monomer, 3 rings per P($g_3$2T-T) monomer and 4 rings for PBTTT-C_{12}/C_{14} and P(g_3BTTT). A density of 1.1 g/cm^3 was reported for P3HT and PBTTT [58, 67]. For the other polymers, the same density was assumed. The thiophene unit density is the product of the Avogadro constant (N_A), the polymer density (ρ_{pol}, in g/cm^3) and the rings per monomer (N_{TU}), divided by the molar mass of a repeating unit (M_R). The charge per TU was calculated by dividing $[Charge]_{tot}$ by the TU density, and corrected for the change in thickness upon doping ($d_{doped}/d_{undoped}$), as ρ_{pol} refers to the undoped film and $[Charge]_{tot}$ to the doped film:

$$Charge/TU = \frac{([Charge]_{tot}) \cdot M_R \cdot d_{doped}}{N_A \cdot \rho_{pol} \cdot N_{TU} \cdot d_{undoped}}$$

4.7 | THz Spectroscopy in Doped Polymer Films

To determine the short-range conductivity (σ_{short}) of the doped polymer films at THz frequencies, we used time-domain THz spectroscopy. A regenerative-amplified Ti:sapphire amplifier laser system (Coherent Astrella) generated pulses (~35 fs) with a center wavelength of 800 nm and an energy of ~ 6 mJ. Part of the fundamental beam was focused onto a non-centrosymmetric 2 mm [110] ZnTe generation crystal to generate the THz pulses of ~1 ps time duration via second-order non-linear optical rectification. The THz pulses were then focused onto the sample via two off-axis parabolic mirrors. For the detection, electro-optic sampling was used in a second 1 mm [110] ZnTe crystal, where the THz pulses were overlapped with an 800 nm gate beam. By changing the time delay between the gate and the THz pulse via a delay line, the THz waveform was recorded. The ZnTe generation crystal, sample and the detector were kept in dry air to exclude THz absorption by ambient humidity. For the doped films, the THz electric field transmitted through the substrate and through the substrate plus film were measured to calculate the complex THz conductivity spectra [68]. At least three measurements were taken at different positions.

The Drude-Smith model (DSM) was fit the complex conductivity spectra ($\tilde{\sigma}(\omega)$):

$$\tilde{\sigma}\ (\omega) = \frac{\varepsilon_0 \omega_P^2 \tau_{DSM}}{(1 - i\omega\tau_{DSM})}\left[1 + \frac{C_{DSM}}{1 - i\omega\tau_{DSM}}\right]$$

Here, ε_0 is the permittivity in free space, ω_P the plasma frequency, τ_{DSM} the scattering time and C_{DSM} the localization parameter. The

plasma frequency ω_P was related to the density of conductive charge ($[Charge]_{DSM}$) as follows:

$$\omega_P^2 = \frac{[Charge]_{DSM} e^2}{\varepsilon_0 m^*}$$

Here, m^* is the effective mass and e the elemental charge. The effective THz mobility (μ_{DSM}) was calculated by using the following formula with $m^* \approx 1.7\ m_e$ (electron mass), as used for P3HT and PBTTT before [22, 69]:

$$\mu_{DSM} = \frac{e\tau_{DSM}}{m^*}\ (1 + C_{DSM})$$

4.8 | Error Propagation

The uncertainties shown in Table S1 and Table 2 were propagated (see equations below) from the standard deviation of the film thickness and sheet resistance measured over 5–10 positions on each film. The uncertainty on $[Charge]_{tot}$ was estimated to ±20%, based on the assumptions in determining the absorbance cross sections and the fitting errors when decomposing the spectra. This is largely a systematic error for each polymer, so that trends of $[Charge]_{tot}$ and μ_{long} within each doped polymer series are reliable.

Long-range conductivity: $\sigma_{long} = \frac{1}{R_S \cdot d}$, with R_S and d denoting sheet resistance and thickness, respectively.

$$\Delta\sigma_{long} = \sqrt{\left(-\frac{1}{R_S^2 \cdot d}\right)^2 (\Delta R_S)^2 + \left(-\frac{1}{R_S \cdot d^2}\right)^2 (\Delta d)^2}$$

Long-range mobility: $\mu_{long} = \frac{\sigma_{long}}{[Charge]_{tot} \cdot e}$, with the conductivity σ_{long}, the total density of charges $[Charge]_{tot}$, and the elementary charge $e = 1.602 \cdot 10^{-19}$ C.

$$\Delta\mu_{long} = \sqrt{\left(\frac{1}{[Charge]_{tot} \cdot e}\right)^2 (\Delta\sigma_{long})^2 + \left(-\frac{\sigma_{long}}{[Charge]_{tot}^2 \cdot e}\right)^2 ([Charge]_{tot})^2}$$

Film thickness increase: $\Delta d/d = \frac{d_{doped} - d_{undoped}}{d_{undoped}}$, with d_{doped} and $d_{undoped}$ being the doped and undoped thickness, respectively.

$$\Delta d/d = \sqrt{\left(\frac{1}{d_{neat}}\right)^2 (\Delta d_{doped})^2 + \left(-\frac{d_{doped}}{d_{neat}^2}\right)^2 (\Delta d_{neat})^2}$$

Short-range conductivity: $\sigma_{short} \sim \frac{1}{d_{doped}}$, approximately, with σ_{mean} being the mean value of different spots with a standard deviation from this value of stdev(σ_{mean}).

$$\Delta\sigma_{short} = \sqrt{\left(\left(-\frac{\sigma_{mean}}{d_{doped}}\right) \cdot \Delta d_{doped}\right)^2 + \text{stdev}(\sigma_{mean})^2}$$

Distance resilience = $\frac{\sigma_{long}}{\sigma_{short}}$, with σ_{long} and σ_{short} being the long-range and short-range conductivity, respectively.

$$\Delta\text{Distance resilience} = \sqrt{\left(\frac{1}{\sigma_{short}}\right)^2 (\Delta\sigma_{long})^2 + \left(-\frac{\sigma_{long}}{\sigma_{short}^2}\right)^2 (\Delta\sigma_{short})^2}$$

4.9 | Grazing-Incidence Wide-Angle X-Ray Scattering (GIWAXS) Measurements

Polymer films were prepared on 1.5 cm × 1.5 cm pre-cleaned Si substrates and doped with the same methods as described above (see Figures S23–S26 for detailed conditions). The cleaning was also identical with the exception of plasma-etching for 10 min instead of UV-ozone cleaning. We note that a different batch of P(g_3BTTT) and P($g_3$2T-T) was used than the rest of the manuscript, which showed similar conductivities and trends. Ex-situ GIWAXS measurements were conducted at Stanford Synchrotron Radiation Lightsource (SSRL) Beamline 11–3 using incidence x-ray energy of 12.7 keV, 250 mm detector distance, 0.12° incidence angle in a He-chamber. 90 s of total exposure time was used. The 2D images were calibrated and analyzed by using Igor Pro with Nika and GIWAXSTools macros. The 0–89 chi angle range was used to produce full radial-integrated 1D plots, then baselined with fourth order polynomial functions. Full-integrated plots were used to calculate (100) peak area, (010) d-spacing and (010) paracrystalline disorder. The paracrystalline disorder (g), was calculated using:

$$g = \sqrt{\frac{\Delta q}{2\pi q_c}}$$

Author Contributions

B.H. acquired and analyzed the optical and transport data for P(g_3BTTT), PBTTT-C_{14} and P3HT, performed the spectro-electrochemistry measurements for all polymers, interpreted the experimental results and wrote a draft of the manuscript. M.M.H. performed the optical and transport measurements for P($g_3$2T-T) and analyzed the results. E.R. performed optical and transport measurements for P3HT, and the temperature-dependent transport measurements. L.B. and J.V. synthesized the P(g_3BTTT) and PBTTT-C_{14} polymers (and the P($g_3$2T-T) batch used for GIWAXS) under the supervision of W.M. D.R. and J.V. assisted in the GIWAXS analysis and helped in the writing of the GIWAXS part. C.K. synthesized the P($g_3$2T-T) polymer under the supervision of I.M. S.G. performed the optical and transport measurements for PBTTT-C_{12}. O.B. helped with the writing of the paper. N.A.-K. performed the GIWAXS measurements, analysis and writing of the GIWAXS part under the supervision of S.H.T. DT performed optical and transport measurements on P3HT, helped with the data analysis, participated in writing the manuscript and supervised the project. N.B. supervised the experimental work, was in charge of the overall project and finalized the manuscript. All authors contributed to the revision and editing of the manuscript.

Acknowledgements

This project received funding from the European Union's Horizon 2020 research and innovation program under grant agreement no. 964677 (MITICS). B.H, M.M.H., E.R., S.G., O.B and N.B. thank the Swiss National

Science Foundation (SNSF, grant 200020_215384) and the University of Bern for funding. B.H., N.B. and W.M. thank the Weave SNSF-FWO Vlaanderen program (Grant 200021E_205216, G025922N) for financial support. L.B. and W.M. thank the FWO Vlaanderen for financial support (Ph.D. Grant 1S70122N). N.A.K. and S.H.T. thank the National Science Foundation under Award DMR-2513790. Use of the Stanford Synchrotron Radiation Lightsource (SSRL), SLAC National Accelerator Laboratory, is supported by the U.S. Department of Energy, Office of Science, Office of Basic Energy Sciences under Contract No. DE-AC02-76SF00515. We thank Benjamin J. Schwartz and Diego Garcia Vidales from University of California, Los Angeles for helping with GIWAXS. We thank SSRL for the use of Beamline 11–3.

Open access publishing facilitated by Universitat Bern, as part of the Wiley - Universitat Bern agreement via the Consortium Of Swiss Academic Libraries.

Conflicts of Interest

The authors declare no conflicts of interest.

Data Availability Statement

The data that support the findings of this work are available as open access in the BORIS Repository of the University of Bern at DOI: https://doi.org/10.48620/96566.

References

1. S. H. Wang, G. Z. Zuo, J. Kim, and H. Sirringhaus, "Progress of Conjugated Polymers as Emerging Thermoelectric Materials," *Progress in Polymer Science* 129 (2022): 101548, https://doi.org/10.1016/j.progpolymsci.2022.101548.

2. G. Bidan and G. Bidan, "Electroconducting Conjugated Polymers: New Sensitive Matrices to Build Up Chemical or Electrochemical Sensors. A Review," *Sensors and Actuators B: Chemical* 6 (1992): 45–56, https://doi.org/10.1016/0925-4005(92)80029-W.

3. B. Lüssem, M. Riede, and K. Leo, "Doping of Organic Semiconductors," *Physica Status Solidi (a)* 210 (2012): 9–43, https://doi.org/10.1002/pssa.201228310.

4. A. I. Hofmann, R. Kroon, S. Zokaei, et al., "Chemical Doping of Conjugated Polymers With the Strong Oxidant Magic Blue," *Advanced Electronic Materials* 6 (2020): 2000249, https://doi.org/10.1002/aelm.202000249.

5. J. Tang, Y.-H. Pai, and Z. Liang, "Strategic Insights Into Semiconducting Polymer Thermoelectrics by Leveraging Molecular Structures and Chemical Doping," *ACS Energy Letters* 7 (2022): 4299–4324, https://doi.org/10.1021/acsenergylett.2c02119.

6. Y. Yamashita, J. Tsurumi, M. Ohno, et al., "Efficient Molecular Doping of Polymeric Semiconductors Driven by Anion Exchange," *Nature* 572 (2019): 634–638, https://doi.org/10.1038/s41586-019-1504-9.

7. I. E. Jacobs, G. D'Avino, V. Lemaur, et al., "Structural and Dynamic Disorder, Not Ionic Trapping, Controls Charge Transport in Highly Doped Conducting Polymers," *Journal of the American Chemical Society* 144 (2022): 3005–3019, https://doi.org/10.1021/jacs.1c10651.

8. E. M. Thomas, K. A. Peterson, A. H. Balzer, et al., "Effects of Counter-Ion Size on Delocalization of Carriers and Stability of Doped Semiconducting Polymers," *Advanced Electronic Materials* 6 (2020): 2000595, https://doi.org/10.1002/aelm.202000595.

9. T. L. Murrey, M. A. Riley, G. Gonel, et al., "Anion Exchange Doping: Tuning Equilibrium to Increase Doping Efficiency in Semiconducting Polymers," *The Journal of Physical Chemistry Letters* 12 (2021): 1284–1289, https://doi.org/10.1021/acs.jpclett.0c03620.

10. S. Watanabe, R. Hakamatani, K. Yaegashi, et al., "Surface Doping of Organic Single-Crystal Semiconductors to Produce Strain-Sensitive Conductive Nanosheets," *Advanced Science* 8 (2021): 2002065, https://doi.org/10.1002/advs.202002065.

11. S. Kohno, Y. Yamashita, N. Kasuya, et al., "Controlled Steric Selectivity in Molecular Doping Towards Closest-Packed Supramolecular Conductors," *Communications Materials* 1 (2020): 79, https://doi.org/10.1038/s43246-020-00081-3.

12. W. Zhao, J. Ding, Y. Zou, C. A. Di, and D. Zhu, "Chemical Doping of Organic Semiconductors for Thermoelectric Applications," *Chemical Society Reviews* 49 (2020): 7210–7228, https://doi.org/10.1039/D0CS00204F.

13. I. E. Jacobs, Y. Lin, Y. Huang, et al., "High-Efficiency Ion-Exchange Doping of Conducting Polymers," *Advanced Materials* 34 (2022): 2102988, https://doi.org/10.1002/adma.202102988.

14. M. Comin, S. Fratini, X. Blase, and G. D'Avino, "Doping-Induced Dielectric Catastrophe Prompts Free-Carrier Release in Organic Semiconductors," *Advanced Materials* 34 (2022): 2105376, https://doi.org/10.1002/adma.202105376.

15. M. Koopmans, M. A. T. Leiviskä, J. Liu, et al., "Electrical Conductivity of Doped Organic Semiconductors Limited by Carrier–Carrier Interactions," *ACS Applied Materials & Interfaces* 12 (2020): 56222–56230, https://doi.org/10.1021/acsami.0c15490.

16. X. Yang, G. Ye, J. Liu, R. C. Chiechi, and L. J. A. Koster, "Carrier–Carrier Repulsion Limits the Conductivity of N-Doped Organic Semiconductors," *Advanced Materials* 36 (2024): 2404397, https://doi.org/10.1002/adma.202404397.

17. K. G. Cho, D. Z. Adrahtas, K. H. Lee, and C. D. Frisbie, "Sub-Band Filling and Hole Transport in Polythiophene-Based Electrolyte-Gated Transistors: Effect of Side-Chain Length and Density," *Advanced Functional Materials* 33 (2023): 2303700, https://doi.org/10.1002/adfm.202303700.

18. D. Tsokkou, P. Cavassin, G. Rebetez, and N. Banerji, "Bipolarons Rule the Short-Range Terahertz Conductivity in Electrochemically Doped P3HT," *Materials Horizons* 9 (2022): 482–491, https://doi.org/10.1039/D1MH01343B.

19. D. Neusser, C. Malacrida, M. Kern, Y. M. Gross, J. van Slageren, and S. Ludwigs, "High Conductivities of Disordered P3HT Films by an Electrochemical Doping Strategy," *Chemistry of Materials* 32 (2020): 6003–6013, https://doi.org/10.1021/acs.chemmater.0c01293.

20. P. Cavassin, I. Holzer, D. Tsokkou, O. Bardagot, J. Rehault, and N. Banerji, "Electrochemical Doping in Ordered and Disordered Domains of Organic Mixed Ionic–Electronic Conductors," *Advanced Materials* 35 (2023): 2300308, https://doi.org/10.1002/adma.202300308.

21. D. Neusser, X. Sun, S. S. Jena, et al., "Electrochemical Doping for Absorption and Conductivity Tuning of P (NDI2OD-T2) Films," *Advanced Electronic Materials* 11 (2025): 70124, https://doi.org/10.1002/aelm.70124.

22. J. E. Northrup, "Atomic and electronic structure of polymer organic semiconductors: P3HT, PQT, and PBTTT," *Physical Review B* 76 (2007): 245202, https://doi.org/10.1103/PhysRevB.76.245202.

23. I. McCulloch, M. Heeney, C. Bailey, et al., "Liquid-Crystalline Semiconducting Polymers With High Charge-Carrier Mobility," *Nature Materials* 5 (2006): 328–333, https://doi.org/10.1038/nmat1612.

24. D. Alberga, A. Perrier, I. Ciofini, G. F. Mangiatordi, G. Lattanzi, and C. Adamo, "Morphological and Charge Transport Properties of Amorphous and Crystalline P3HT and PBTTT: Insights From Theory," *Physical Chemistry Chemical Physics* 17 (2015): 18742–18750, https://doi.org/10.1039/C5CP02769A.

25. E. Röck, D. Tsokkou, B. Hunger, et al., "Distance–Resilient Conductivity in p-Doped Polythiophenes," *Materials Horizons* 12 (2025): 10827–10838, https://doi.org/10.1039/D5MH00620A.

26. K. A. Peterson, E. M. Thomas, and M. L. Chabinyc, "Thermoelectric Properties of Semiconducting Polymers," *Annual Review of Materials Research* 50 (2020): 551–574, https://doi.org/10.1146/annurev-matsci-082219-024716.

27. R. K. Hallani, B. D. Paulsen, A. J. Petty, et al., "Regiochemistry-Driven Organic Electrochemical Transistor Performance Enhancement

in Ethylene Glycol-Functionalized Polythiophenes," *Journal of the American Chemical Society* 143 (2021): 11007–11018, https://doi.org/10.1021/jacs.1c03516.

28. W. Y. Gao and A. Kahn, "Controlled p -Doping of Zinc Phthalocyanine by Coevaporation With Tetrafluorotetracyanoquinodimethane: A Direct and Inverse Photoemission Study," *Applied Physics Letters* 79 (2001): 4040–4042, https://doi.org/10.1063/1.1424067.

29. Y. H. Zhong, V. Untilova, D. Muller, et al., "Preferential Location of Dopants in the Amorphous Phase of Oriented Regioregular Poly(3-hexylthiophene-2,5-diyl) Films Helps Reach Charge Conductivities of 3000 S cm^{-1}," *Advanced Functional Materials* 32 (2022): 2202075, https://doi.org/10.1002/adfm.202202075.

30. A. Dash, S. Guchait, D. Scheunemann, et al., "Spontaneous Modulation Doping in Semi-Crystalline Conjugated Polymers Leads to High Conductivity at Low Doping Concentration," *Advanced Materials* 36 (2024): 2311303, https://doi.org/10.1002/adma.202311303.

31. B. J. Barrett, S. S. Saund, R. A. Dziatko, T. L. Clark-Winters, H. E. Katz, and A. E. Bragg, "Spectroscopic Studies of Charge-Transfer Character and Photoresponses of F_4TCNQ-Based Donor–Acceptor Complexes," *The Journal of Physical Chemistry C* 124 (2020): 9191–9202, https://doi.org/10.1021/acs.jpcc.0c01372.

32. M. Moser, L. R. Savagian, A. Savva, et al., "Ethylene Glycol-Based Side Chain Length Engineering in Polythiophenes and its Impact on Organic Electrochemical Transistor Performance," *Chemistry of Materials* 32 (2020): 6618–6628, https://doi.org/10.1021/acs.chemmater.0c02041.

33. J. Hynynen, D. Kiefer, L. Yu, et al., "Enhanced Electrical Conductivity of Molecularly p-Doped Poly(3-hexylthiophene) Through Understanding the Correlation With Solid-State Order," *Macromolecules* 50 (2017): 8140–8148, https://doi.org/10.1021/acs.macromol.7b00968.

34. K. Szendrei, D. Jarzab, Z. H. Chen, A. Facchetti, and M. A. Loi, "Ambipolar All-Polymer Bulk Heterojunction Field-Effect Transistors," *Journal of Materials Chemistry* 20 (2010): 1317–1321, https://doi.org/10.1039/B919596C.

35. V. Vijayakumar, E. Zaborova, L. Biniek, et al., "Effect of Alkyl Side Chain Length on Doping Kinetics, Thermopower, and Charge Transport Properties in Highly Oriented F4TCNQ-Doped PBTTT Films," *ACS Applied Materials & Interfaces* 11 (2019): 4942–4953, https://doi.org/10.1021/acsami.8b17594.

36. T. L. Murrey, M. Berteau-Rainville, G. Gonel, et al., "Quantifying Polaron Densities in Sequentially Doped Conjugated Polymers: Exploring the Upper Limits of Molecular Doping and Conductivity," *Journal of Materials Chemistry C* 11 (2023): 14884–14895, https://doi.org/10.1039/D3TC01569F.

37. D. Neusser, C. Malacrida, M. Kern, Y. M. Gross, J. van Slageren, and S. Ludwigs, "High Conductivities of Disordered P3HT Films by an Electrochemical Doping Strategy," *Chemistry of Materials* 32 (2020): 6003–6013, https://doi.org/10.1021/acs.chemmater.0c01293.

38. Z. Wang, "Characterization and Optimization of the Electrical Conductivity of a Semi-Crystalline Conjugated Polymer PBTTT upon Doping," *Journal of Physics: Conference Series* 1635 (2020): 012037, https://doi.org/10.1088/1742-6596/1635/1/012037.

39. C. Chen, I. E. Jacobs, K. Kang, et al., "Observation of Weak Counterion Size Dependence of Thermoelectric Transport in Ion Exchange Doped Conducting Polymers Across a Wide Range of Conductivities," *Advanced Energy Materials* 13 (2023): 2202797, https://doi.org/10.1002/aenm.202202797.

40. J. Park, J. H. Song, J. G. Jang, and J. Kwak, "High Conductivity in PEDOT: PSS Thin-Films by Secondary Doping with Superacid Vapor: Mechanisms and Application to Thermoelectrics," *Advanced Physics Research* 4 (2025): 2400151, https://doi.org/10.1002/apxr.202400151.

41. Z. Ke, J. Chaudhary, L. Q. Flagg, et al., "Controlled Dedoping and Redoping of N-Doped Poly(benzodifurandione) (n-PBDF)," *Advanced Functional Materials* 34 (2024): 2400255, https://doi.org/10.1002/adfm.202400255.

42. Z. Ke, A. Abtahi, J. Hwang, et al., "Highly Conductive and Solution-Processable n-Doped Transparent Organic Conductor," *Journal of the American Chemical Society* 145 (2023): 3706–3715, https://doi.org/10.1021/jacs.2c13051.

43. W. Cui, Q. Jiang, X. He, et al., "Charge Transport Properties of PBFDO at Various Doping Levels: An Electrochemical Control and Hall Effect Characterization Study," *The Journal of Physical Chemistry Letters* 16 (2025): 6393–6401, https://doi.org/10.1021/acs.jpclett.5c01300.

44. K. Xu, T.-P. Ruoko, M. Shokrani, et al., "On the Origin of Seebeck Coefficient Inversion in Highly Doped Conducting Polymers," *Advanced Functional Materials* 32 (2022): 2112276, https://doi.org/10.1002/adfm.202112276.

45. A. J. Moulé, G. Gonel, T. L. Murrey, et al., "Quantifying polaron mole fractions and interpreting spectral changes in molecularly doped conjugated polymers," *Advanced Electronic Materials* 8 (2021): 2100888, https://doi.org/10.1002/aelm.202100888.

46. I. Sahalianov, J. Hynynen, S. Barlow, S. R. Marder, C. Muller, and I. Zozoulenko, "UV-to-IR Absorption of Molecularly p-Doped Polythiophenes With Alkyl and Oligoether Side Chains: Experiment and Interpretation Based on Density Functional Theory," *The Journal of Physical Chemistry B* 124 (2020): 11280–11293, https://doi.org/10.1021/acs.jpcb.0c08757.

47. C. Enengl, S. Enengl, S. Pluczyk, et al., "Doping-Induced Absorption Bands in P3HT: Polarons and Bipolarons," *Chemphyschem* 17 (2016): 3836–3844, https://doi.org/10.1002/cphc.201600961.

48. R. Ghosh and F. C. Spano, "Excitons and Polarons in Organic Materials," *Accounts of Chemical Research* 53 (2020): 2201–2211, https://doi.org/10.1021/acs.accounts.0c00349.

49. P. Rapta, J. Lukkari, J. Tarábek, et al., "Ultrathin Polyelectrolyte Multilayers: In Situ ESR/UV-Vis-NIR Spectroelectrochemical Study of Charge Carriers Formed Under Oxidation," *Physical Chemistry Chemical Physics* 6 (2004): 434–441, https://doi.org/10.1039/B308891J.

50. D. Kiefer, R. Kroon, A. I. Hofmann, et al., "Double Doping of Conjugated Polymers With Monomer Molecular Dopants," *Nature Materials* 18 (2019): 149–155, https://doi.org/10.1038/s41563-018-0263-6.

51. D. T. Duong, C. C. Wang, E. Antono, M. F. Toney, and A. Salleo, "The Chemical and Structural Origin of Efficient p-Type Doping in P3HT," *Organic Electronics* 14 (2013): 1330–1336, https://doi.org/10.1016/j.orgel.2013.02.028.

52. D. Derewjanko, D. Scheunemann, E. Järsvall, A. I. Hofmann, C. Müller, and M. Kemerink, "Delocalization Enhances Conductivity at High Doping Concentrations," *Advanced Functional Materials* 32 (2022): 2112262, https://doi.org/10.1002/adfm.202112262.

53. I. E. Jacobs, Y. Lin, Y. Huang, et al., "High-Efficiency Ion-Exchange Doping of Conducting Polymers," *Advanced Materials* 34 (2022): 2102988, https://doi.org/10.1002/adma.202102988.

54. M. L. Tietze, J. Benduhn, P. Pahner, et al., "Elementary Steps in Electrical Doping of Organic Semiconductors," *Nature Communications* 9 (2018): 1182, https://doi.org/10.1038/s41467-018-03302-z.

55. S. Guchait, A. Dash, A. Lemaire, L. Herrmann, M. Kemerink, and M. Brinkmann, "Phase-Selective Doping of Oriented Regioregular Poly (3-hexylthiophene-2, 5-diyl) Controls Stability of Thermoelectric Properties," *Advanced Functional Materials* 34 (2024): 2404411, https://doi.org/10.1103/PhysRevB.87.115209.

56. P. Pingel and D. Neher, "Comprehensive Picture of p-Type Doping of P3HT With the Molecular Acceptor F_4TCNQ," *Physical Review B* 87 (2013): 115209, https://doi.org/10.1103/PhysRevB.87.115209.

57. J. Mårdalen, E. J. Samuelsen, O. R. Gautun, and P. H. Carlsen, "X-ray Scattering From Oriented Poly(3-alkylthiophenes)," *Synthetic Metals* 48 (1992): 363–380, https://doi.org/10.1016/0379-6779(92)90239-F.

58. D. R. Kozub, K. Vakhshouri, S. V. Kesava, C. Wang, A. Hexemer, and E. D. Gomez, "Direct Measurements of Exciton Diffusion Length Limita-

tions on Organic Solar Cell Performance," *Chemical Communications* 48 (2012): 5859–5861, https://doi.org/10.1039/C2CC31925J.

59. M. J. Sher, J. A. Bartelt, T. M. Burke, A. Salleo, M. D. McGehee, and A. M. Lindenberg, "Time- and Temperature-Independent Local Carrier Mobility and Effects of Regioregularity in Polymer-Fullerene Organic Semiconductors," *Advanced Electronics Materials* 2 (2016): 1500351, https://doi.org/10.1002/adfm.201700173.

60. J. E. Cochran, M. J. N. Junk, A. M. Glaudell, et al., "Molecular Interactions and Ordering in Electrically Doped Polymers: Blends of PBTTT and F_4TCNQ," *Macromolecules* 47 (2014): 6836–6846, https://doi.org/10.1021/ma501547h.

61. V. Skrypnychuk, N. Boulanger, V. Yu, et al., "Enhanced Vertical Charge Transport in a Semiconducting P3HT Thin Film on Single Layer Graphene," *Advanced Functional Materials* 25 (2014): 664–670, https://doi.org/10.1002/adfm.201403418.

62. M. Craighero, J. Guo, S. Zokaei, et al., "Impact of Oligoether Side-Chain Length on the Thermoelectric Properties of a Polar Polythiophene," *ACS Applied Electronic Materials* 6 (2024): 2909–2916, https://doi.org/10.1021/acsaelm.3c00936.

63. A. Hamidi-Sakr, L. Biniek, J. L. Bantignies, et al., "A Versatile Method to Fabricate Highly In-Plane Aligned Conducting Polymer Films with Anisotropic Charge Transport and Thermoelectric Properties: The Key Role of Alkyl Side Chain Layers on the Doping Mechanism," *Advanced Functional Materials* 27 (2017): 1700173, https://doi.org/10.1002/adfm.201700173.

64. V. Untilova, H. Zeng, P. Durand, L. Herrmann, N. Leclerc, and M. Brinkmann, "Intercalation and Ordering of F_6TCNNQ and F_4TCNQ Dopants in Regioregular Poly(3-hexylthiophene) Crystals: Impact on Anisotropic Thermoelectric Properties of Oriented Thin Films," *Macromolecules* 54 (2021): 6073–6084, https://doi.org/10.1021/acs.macromol.1c00554.

65. J. Vanderspikken, Q. Liu, Z. Liu, et al., "Tuning Electronic and Morphological Properties for High-Performance Wavelength-Selective Organic Near-Infrared Cavity Photodetectors," *Advanced Functional Materials* 32 (2021): 2108146, https://doi.org/10.1002/adfm.202108146.

66. L. Bynens, K. Zhang, P. Cavassin, et al., "Organic Electrochemical Transistor Channel Materials: Copolymerization Versus Physical Mixing of Glycolated and Alkoxylated Polymers," *Advanced Functional Materials* 36 (2025): 2423913, https://doi.org/10.1002/adfm.202423913.

67. C. S. Lee and M. D. Dadmun, "Important Thermodynamic Characteristics of Poly(3-Hexyl Thiophene)," *Polymer* 55 (2014): 4–7, https://doi.org/10.1016/j.polymer.2013.11.033.

68. J. C. Brauer, V. K. Thorsmolle, and J. E. Moser, "Terahertz Time-Domain Spectroscopy Study of the Conductivity of Hole-Transporting Materials," *Chimia* 63 (2009): 189–192, https://doi.org/10.2533/chimia.2009.189.

69. P. Krauspe, D. Tsokkou, M. Causa, et al., "Terahertz Short-Range Mobilities in Neat and Intermixed Regions of Polymer:Fullerene Blends With Controlled Phase Morphology," *Journal of Materials Chemistry A* 6 (2018): 22301–22309, https://doi.org/10.1039/C8TA08061E.

Supporting Information

Additional supporting information can be found online in the Supporting Information section.

Supporting File: adma72964-sup-0001-SuppMat.pdf.